SPECIAL TOPIC — A 40th Anniversary Celebration: Physics Research and Innovation at Ningbo University

Hydrogen-mediated enhancement of Ag_4 cluster activity and stability for CO_2 electroreduction

Ziyuan Li(李梓源)[†], Yunhan Wang(王韵含)[†], Shan Gao(高姗)[‡], and Xiangmei Duan(段香梅)[§]

School of Physical Science and Technology, Ningbo University, Ningbo 315211, *China*

(Received 2 June 2026; revised manuscript received 25 July 2026; accepted manuscript online 17 August 2026)

Electrochemical CO_2 reduction to CO (CO_2RR) is a sustainable carbon utilization route. Silver is widely recognized for its high CO selectivity and favorable cost-performance compared to gold, but nanostructured Ag catalysts suffer from stability issues during prolonged operation. Using the IM^{2}ODE inverse-design algorithm and density functional theory calculations, we identify the large-pore N-doped graphene (NG) supported regular tetrahedral Ag_4 cluster (r-Tet) as thermodynamically stable and CO_2RR-active. Substituting its apical Ag atom (Ag_3M@NG; M = Cu, Ru, Rh, Pd, Ir, Pt, Au) shows that coinage metals (Cu, Au) preserve stability but lack activity, whereas other metals cause loss of the initial tetrahedral geometry due to excessive CO binding (−2.63 eV to −3.20 eV). To resolve this, we introduce a hydrogen atom at the hollow site (Hollow-H) of r-Tet, which concurrently activates the Ag_4 cluster for CO_2RR and strengthens interfacial Ag–N bonding. The H-activated catalyst proceeds via a two-stage mechanism with H activation (0.80 eV) as the potential-determining step (PDS). Crucially, Hollow-H acts as a dual-purpose electronic promoter: It localizes the apical Ag atom orbital for CO_2 activation while simultaneously transferring charge to prevent cluster deformation from an imbalanced charge distribution. This work establishes hydrogen-activated engineering as a general strategy for enhancing both the activity and stability of supported cluster electrocatalysts.

Keywords: density functional theory, CO_2RR, silver-based catalysts, hydrogen-charge buffer

PACS: 71.15.Mb, 82.45.Jn, 36.40.Jn, 73.20.At

DOI: 10.1088/1674-1056/ae9a61 **CSTR:** 32038.14.CPB.ae9a61

1. Introduction

Converting waste CO_2 to CO using renewable electricity and feeding the product into existing syngas processes is a viable route for a "green carbon" cycle.[1–5] The electrochemical CO_2 reduction to CO (CO_2RR) is particularly attractive due to its two-electron, two-product nature, which offers favorable kinetics. Silver is a leading catalyst candidate because it balances moderate COOH binding (*COOH), weak CO adsorption (*CO), and relatively low cost compared to Au.[6–9] However, Ag-based catalysts face two coupled challenges: The weak CO_2 adsorption leads to a high overpotential for *COOH formation (the potential-determining step),[10,11] while structural degradation (aggregation, dissolution, and surface reconstruction) under extended operation limits durability.[12–14] Moreover, strategies that boost activity often compromise stability, and vice versa, creating a persistent activity-stability trade-off that must be overcome for practical application.[15,16]

Nano-structuring of metal catalysts reduces their characteristic dimensions to the nanoscale or even sub-nanometer regime, thereby substantially increasing the specific surface area and the number of under-coordinated surface atoms, and tailoring electronic structures through quantum effects.[17,18] Fully realizing these benefits often necessitates an appropriate support, particularly two-dimensional (2D) nitrogen-doped carbon-based materials, where electron-rich N sites stabilize metal clusters via strong metal–support interactions while modulating the electronic structure of active sites.[19–21] Experimentally, Ag atomic clusters on N-doped carbon nanotubes have achieved CO Faradaic efficiencies exceeding 99% for CO_2 electroreduction.[19] Bai *et al.*[22] demonstrated that Cu_3 clusters on g-C_3N_4, where each Cu atom coordinates to pyridinic N, exhibit delocalized Cu d-orbital states arising from Cu–N hybridization; P and Se heteroatom engineering was employed to re-tune the electronic structure for selective CO_2-to-ethylene conversion. Zhang *et al.*[23] screened M_4 clusters on C_2N and found that Cr_4 and Mn_4 achieve limiting potentials of −0.24 V and −0.23 V for CO production, outperforming their single-atom counterparts. For Ag specifically, Zhang *et al.*[24] compared Ag_4, Ag_8, and Ag_{13} on g-C_3N_4 and demonstrated that Ag_4 exhibits the strongest CO_2 chemisorption among the three sizes. These studies collectively underscore the sensitivity of catalytic performance to cluster and coordination geometry, yet strategies for simultaneously enhancing the activity and structural stability of supported Ag four-atom clusters under reaction conditions remain

[†]These authors contributed equally to this work

[‡]Corresponding author. E-mail: gaoshan@nbu.edu.cn

[§]Corresponding author. E-mail: duanxiangmei@nbu.edu.cn

© 2026 Chinese Physical Society and IOP Publishing Ltd. All rights, including for text and data mining, AI training, and similar technologies, are reserved.

CPB Online In-Press

largely unexplored.

A critical aspect that remains underexplored is the role of the aqueous electrochemical environment, specifically adsorbed hydrogen (*H), in modulating both stability and activity. Zhang *et al.*[25] demonstrated that *H adsorption serves as a dominant driving force for Cu catalyst restructuring during CO_2RR by weakening metal-metal bonds and inducing lattice expansion, with the mechanism extending across multiple transition metals. Huang *et al.*[26] further established the charge state of adsorbed *H as a critical kinetic descriptor for hydrogen electrochemistry. Whereas Ag was predicted to resist *H-induced restructuring due to thermodynamically unfavorable H adsorption, the deliberate introduction of hydrogen into the catalyst system may offer a novel route to actively modulate both stability and activity.

Herein, we combine inverse-design structure search with comprehensive density functional theory (DFT) calculations to systematically investigate Ag_4 clusters on N-doped graphene (Ag_4@NG) for CO_2RR. The IM^{2}ODE algorithm[27] identifies the thermodynamically favored cluster configuration and we elucidate its electronic stability origin. Apical-atom substitution (Ag_3M@NG) reveals a divergence between initial-state and reaction-state stability. To resolve the activity-stability dilemma, we propose the Hollow-H strategy and uncover a dynamic charge-buffer mechanism, an electronic effect in which H-induced polarization simultaneously activates the apical Ag site and reinforces interfacial anchoring. This establishes hydrogen engineering as a generalizable framework for stable, active cluster electrocatalysts.

2. Computational methods

All spin-polarized DFT calculations were performed using the Vienna ab initio simulation package (VASP)[28,29] with the projector augmented wave (PAW) method.[30] The Perdew–Burke–Ernzerhof (PBE) functional within the generalized gradient approximation (GGA) was employed,[31] with the DFT-D3 dispersion correction.[32] A plane-wave energy cutoff of 500 eV and Gamma-centered k-point meshes of $[3\times3\times1]$ (relaxation) and $[7\times7\times1]$ (electronic structure) were used. All structures were relaxed until residual forces fell below 0.03 eV/Å and total energy convergence reached 10^{-5} eV. The NG substrate was modeled using a $7\times7\times1$ graphene supercell ($a=b=17.22$ Å, $c=20.00$ Å; $\alpha=\beta=90^\circ$, $\gamma=120^\circ$) with pyridinic-N-terminated pore edges (diameter ~5.70 Å).

Bader charge analysis[33] was employed to evaluate the charge distribution and electron transfer among the constituent atoms, where positive values indicate electron loss and negative values indicate electron gain. Crystal orbital hamiltonian population (COHP) analysis used the LOBSTER package,[34,35] with integrated COHP (ICOHP) values quantifying bond strength. The IM^{2}ODE single-objective DE search employed a random initial population of 10 Ag_4/NG candidates, a mutation factor of 0.6, duplicate removal after local DFT relaxation and energy ranking. To verify search convergence with respect to generation number, 50 DE generations were conducted, and converged to three low-energy candidate structures. The workflow proceeds as illustrated in Fig. 1 and more explanations regarding IM^{2}ODE are provided in Supplementary Material S1.

The cluster binding energy per atom (E_b) was defined as

$$E_b = (E_{cluster+NG} - E_{cluster} - E_{NG})/n,$$

where $E_{cluster+NG}$, $E_{cluster}$, and E_{NG} are the total energies of the supported cluster system, the isolated cluster, and the substrate, and n is the number of metal atoms in the cluster.

Adsorption energies (E_{ads}) were calculated as

$$E_{ads} = E_{total} - E_{slab} - E_{mol},$$

where E_{total}, E_{slab}, and E_{mol} are the total energy of the slab with adsorbed molecule, the pure slab and the single molecule, respectively.

Reaction free energies followed the computational hydrogen electrode (CHE) model[36]

$$\Delta G = \Delta E + \Delta E_{ZPE} - T\Delta S + \Delta G_{pH} + \Delta G_U,$$

where ΔE represents the reaction energy difference between the reactant and product, which is directly calculated from DFT computations. The zero-point energy (ΔE_{ZPE}) and entropy of the adsorbates are obtained based on the vibrational frequencies and the entropies of the gas phase. ΔG_{pH} and ΔG_U indicate the changes in free energy caused by the variation of H^+ concentration (pH value) and electrode potential (U). The U_L was defined as

$$U_L = -\max(\Delta G)/e,$$

where $\max(\Delta G)$ is the largest positive free energy difference among the elementary steps. The CHE framework provides thermodynamic free energy differences of these proton-coupled electron transfer steps.

Implicit solvation effects were evaluated using VASPsol with EB_K = 80, LAMBDA_D_K = 3.0, and TAU = 0.0. Structural relaxations were performed on the vacuum-optimized geometries. These calculations provide a continuum-solvent thermodynamic reference.

3. Results and discussions

3.1. Inverse design search for stable Ag_4 cluster configurations on N-doped graphene

To identify the thermodynamically stable configuration of Ag_4 clusters in the confined pore of N-doped graphene (NG), we employed the IM^{2}ODE inverse-design algorithm in

CPB Online In-Press

a single-objective optimization to minimize total energy. The NG substrate (Fig. 1, left) was constructed from a $7 \times 7 \times 1$ graphene supercell with pyridinic-N-terminated pore edges, yielding a pore diameter of 5.70 Å, suitable for nanocluster loading. The single-objective optimization was set for 2D-supported cluster geometries with a mutation factor of 0.6. The IM^{2}ODE search followed the standard differential evolution (DE) workflow[27] (Fig. 1, center): (i) generate an initial population of random Ag_4 structures on NG, (ii) locally optimize each candidate with DFT, (iii) rank structures by energy and remove duplicates, and (iv) create new candidates via DE operations.

After structural search and DFT refinement, under our computational conditions, three low-energy Ag_4 configurations emerged (Fig. 1, right). The vertical plate (v-Plt) is a near-planar arrangement oriented perpendicular to the graphene plane; as noted in prior literature, Ag clusters exhibit a propensity for planar geometries in the gas phase and on pristine graphene surfaces.[37–39] The irregular tetrahedron (i-Tet) has a distorted tetrahedral geometry with unequal Ag–Ag and Ag–N bonds. The regular tetrahedron (r-Tet) displays symmetric tetrahedral coordination: Three basal Ag (Ag_b) atoms bond to pore-edge N atoms, while one apical Ag (Ag_a) sits above the basal plane. Average energies per atom are −8.8617 eV/atom, −8.8609 eV/atom, and −8.8602 eV/atom for v-Plt, i-Tet, and r-Tet (Table S1), respectively. Cluster binding energies per Ag atom rank as r-Tet (−1.23 eV) > i-Tet (−1.21 eV) > v-Plt (−1.02 eV). Although average energies differ only by ∼ 1.5 meV/atom, binding energy clearly establishes r-Tet as the most stable configuration.

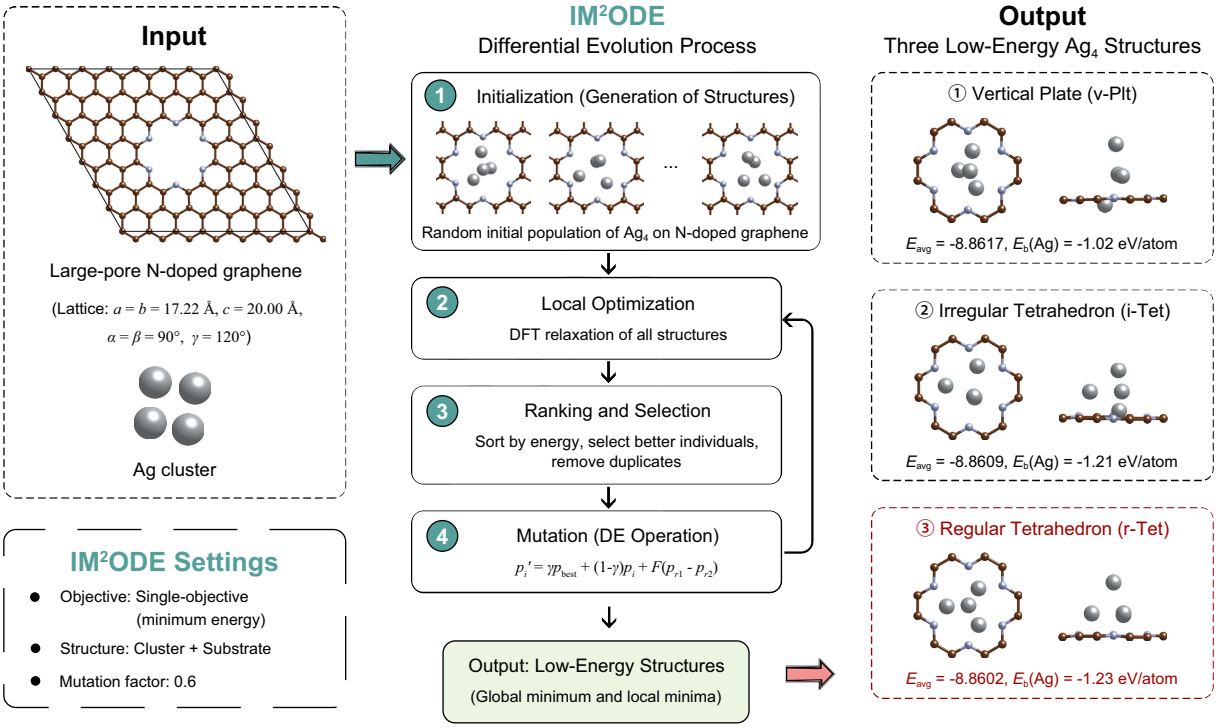


Fig. 1. IM^{2}ODE inverse-design workflow for a stable Ag_4 cluster on N-doped graphene. Left: input structures of the N-doped graphene substrate and the 4-Ag-atom cluster (top), and IM^{2}ODE parameter settings (bottom). Center: four-step DE procedure for structural search. Right: three lowest-energy Ag_4 configurations — vertical plate (v-Plt), irregular tetrahedron (i-Tet), and regular tetrahedron (r-Tet) — with their average total energies per atom and binding energies per Ag atom.

This stability order is notable because Ag clusters typically favor planar shapes, suggesting that the pyridinic-N pore promotes three-dimensional (3D) tetrahedral formation. The preference can be explained geometrically: Three basal Ag atoms maximize bonding with pore-edge N atoms, while an apical Ag completes the tetrahedron. Furthermore, comparison of the projected density of states (PDOS) of the apical Ag atom across the three configurations (Figs. S1–S3) reveals that the d_{z2} orbital of the apical Ag in r-Tet is more localized and lies closer to the Fermi level than those in v-Plt and i-Tet, which is favorable for the subsequent adsorption of electrocatalytic intermediates. Given these geometric and electronic factors, r-Tet was chosen for all further studies.

3.2. Electronic origin of the stability of regular tetrahedral Ag_4 on NG

To elucidate the electronic basis for r-Tet's superior stability, we performed a comprehensive bonding analysis using electron localization function (ELF), charge density difference (CDD), Bader charge analysis, and COHP calculations. The 2D ELF maps (Fig. 2(a)) reveal strong electron localization

(ELF values up to 0.93) near the pyridinic-N pore edge before cluster anchoring, with characteristic red circle areas indicating nitrogen lone-pair electrons. After r-Tet adsorption, the maximum ELF decreases to 0.82 and the red areas diminish, directly evidencing that N lone-pair electrons participate in Ag–N bonding and drive significant interfacial electron redistribution.

The CDD analysis (Fig. 2(b)) confirms electron redistribution in all three configurations, with clear electron accumulation/depletion at the Ag–NG interface. Notably, r-Tet displays more symmetric charge redistribution than the other two, with three Ag_b atoms undergoing comparable charge transfer with coordinating N atoms. Bader charge analysis (Fig. 2(c)) quantifies this homogeneity: v-Plt Ag charges range widely ($-0.41\ e$ to $+1.06\ e$), reflecting heterogeneous coordination; r-Tet charges are narrowly distributed ($-0.37\ e$ to $-0.04\ e$), indicating a homogeneous electronic environment that stabilizes the 3D cluster geometry. i-Tet exhibits intermediate charge heterogeneity, consistent with its intermediate symmetry.

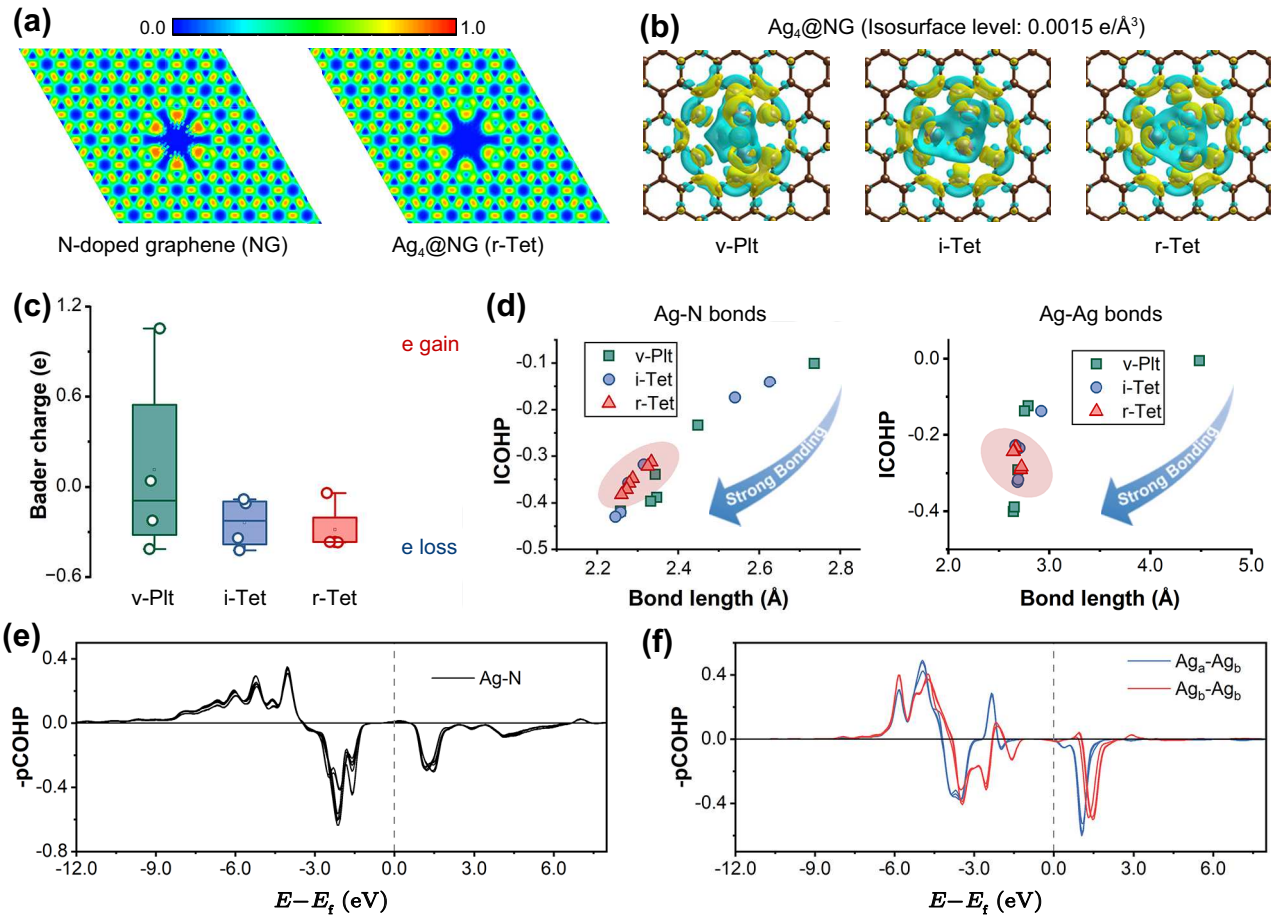


Fig. 2. Electronic origin of r-Tet Ag_4 stability on N-doped graphene. (a) Two-dimensional ELF maps before and after r-Tet adsorption. (b) Charge density difference isosurfaces for v-Plt, i-Tet, and r-Tet. (c) Bader charge distributions of individual Ag atoms. (d) ICOHP versus bond length for Ag–N and Ag–Ag bonds. (e) and (f) –pCOHP curves for six Ag–N bonds and six Ag–Ag bonds in r-Tet (blue: apical-basal Ag–Ag; red: basal-basal Ag–Ag).

ICOHP analysis (Fig. 2(d)) shows the bonding origin of the stability difference. In v-Plt and i-Tet, some bonds are strong (Ag–Ag ICOHP down to −0.40 eV in v-Plt; Ag–N ICOHP down to −0.43 eV in i-Tet), but the overall bonding distributions are broad, with weak bonds (ICOHP near −0.10 eV). This inhomogeneity creates structural weak points. In contrast, r-Tet displays tightly clustered bond strengths: Ag–N ICOHP ranges from −0.38 eV to −0.31 eV, and Ag–Ag ICOHP from −0.29 eV to −0.23 eV. The narrow distributions indicate that r-Tet's stability arises from a balanced network of moderate-strength bonds. The –pCOHP curves (Figs. 2(e) and 2(f)) further support this: The six Ag–N curves nearly overlap, confirming equivalence of the three basal Ag atoms, while Ag–Ag curves separate into two groups — apical-basal (blue) and basal-basal (red).

3.3. Divergent stability regimes and reaction-state instability induced by substitution engineering

Having established r-Tet's stability, we constructed eight Ag_3M@NG systems (M = Cu, Ag, Ru, Rh, Pd, Ir, Pt, Au) by replacing the apical Ag atom to directly modulate the electronic properties of the active center and assess structural sta-

bility. Figure 3a presents the cluster binding energy per atom and Bader charge transfer for each system, revealing two distinct stability regimes. For coinage metals (Cu/Ag/Au), larger binding energies coincide with larger total cluster charge transfer and modest apical-atom charge variation. Here strong Ag–N interactions at the cluster-substrate interface are the primary stability contribution. For the other metals (Ru, Rh, Pd, Ir, Pt), binding energies increase across each period (left to right), while total charge transfer systematically decreases. Instead, binding energy correlates positively with charge variation on the apical M atom: As the M atom accumulates more electron density, binding energy increases. This inverted charge-transfer/binding-energy relationship signals a shift where intra-cluster metal-metal bonding, rather than substrate interaction, governs cluster stability.

Figure 3(b)'s ICOHP bonding balance map plots each system in the space of Ag–N bond strength (–ICOHP(Ag–N)) vs intra-cluster cohesion mismatch ($|\Delta| = |\mathrm{ICOHP}(\mathrm{Ag_b} - M_a) - \mathrm{ICOHP}(\mathrm{Ag_b} - \mathrm{Ag_b})|$). Cu/Ag/Au systems reside in the favorable bottom-left region, characterized by strong Ag–N anchoring and small cohesion mismatch. This indicates balanced, cooperative bonding where interfacial and intra-cluster interactions reinforce each other. The comparable $\mathrm{Ag_b}$–M_a and $\mathrm{Ag_b}$–$\mathrm{Ag_b}$ bond strengths produce a structurally homogeneous cluster with low internal stress and uniform electronic distribution. The other systems are displaced toward the upper-right region, reflecting progressively weaker Ag–N interactions and a growing disparity between $\mathrm{Ag_b}$–M_a and $\mathrm{Ag_b}$–$\mathrm{Ag_b}$ bond strengths. As detailed in Fig. S4, individual ICOHP values confirm that some bonds are excessively strong while others are anomalously weak. A critical consequence of this bonding imbalance is structural deformation under catalytic operating conditions.

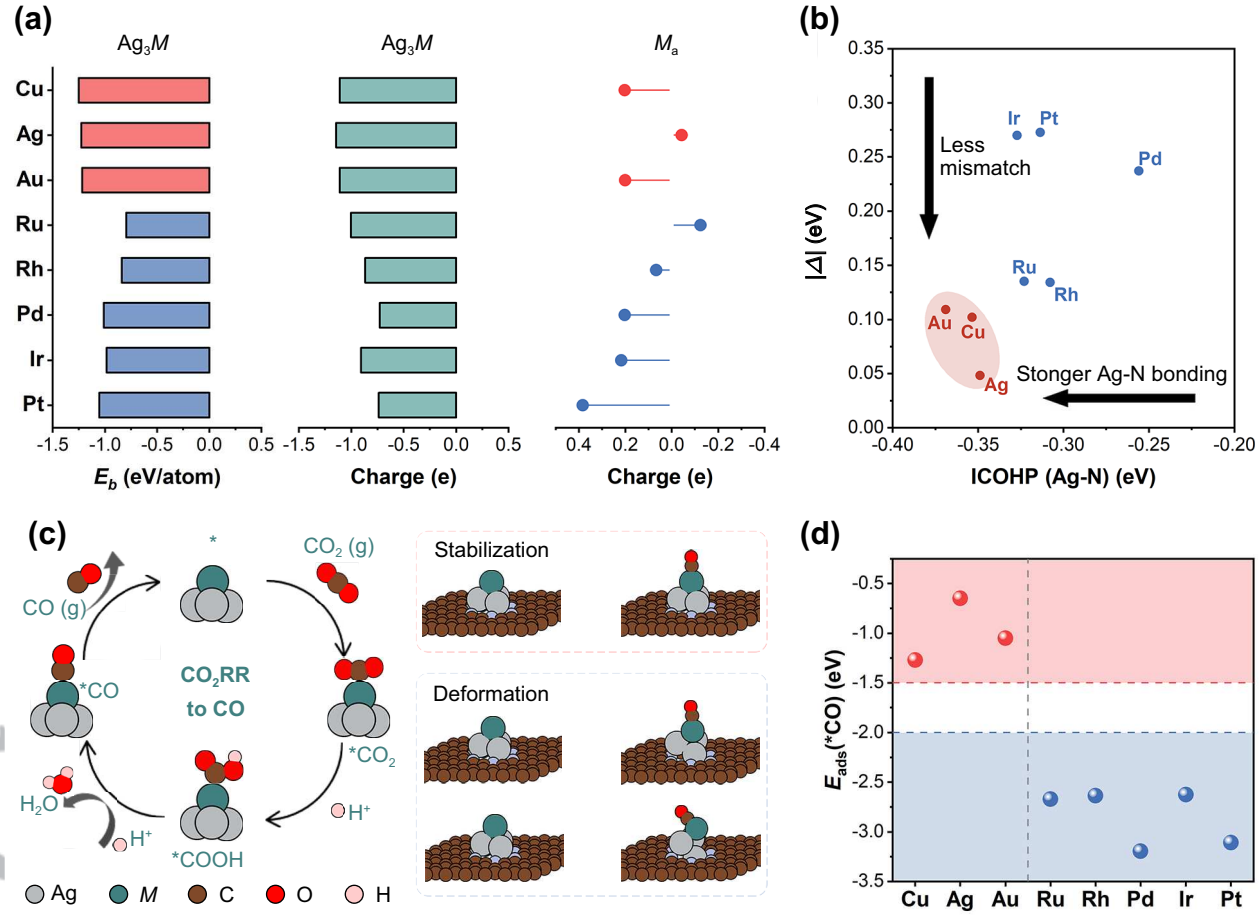


Fig. 3. Stability of $\mathrm{Ag_3}M$@NG (M = Cu, Ag, Au, Ru, Rh, Pd, Ir, Pt) under substitution engineering. (a) Cluster binding energy per atom (left), total cluster Bader charge (center), and apical M atom Bader charge (right). (b) ICOHP bonding balance: intra-cluster cohesion mismatch $|\Delta|$ vs Ag–N bond strength. (c) Left: Standard $\mathrm{CO_2}$RR-to-CO pathway; right: initial- and final-state structures upon *CO adsorption, showing reconstruction from tetrahedral to v-Plt, i-Tet, or r-Tet geometries. (d) *CO adsorption energies for all $\mathrm{Ag_3}M$@NG systems.

Figure 3(c) illustrates the standard $\mathrm{CO_2}$RR-to-CO pathway. In our computational screening, except for the Ru/Ir-substituted systems (which exhibit tilted $\mathrm{CO_2}$ side-on adsorption, Table S2), none of the other $\mathrm{Ag_3}M$@NG systems activate $\mathrm{CO_2}$, which remains physisorbed. CO adsorption (Figs. 3(c) and 3(d)) shows structural differences. Cu/Ag/Au maintain their tetrahedral geometry with moderate CO binding energies (-0.65 eV to -1.27 eV). In contrast, other systems undergo severe structural reconstruction upon *CO adsorption, from rotation into i-Tet-like geometries to complete collapse into v-

Plt configurations, driven by excessively strong *CO binding (−2.63 eV to −3.20 eV). This occurs because *CO adsorption on an already unbalanced cluster exacerbates the cohesion mismatch: The strong *M*–CO bond withdraws electron density from the apical region, effectively pulling the *M* atom away from its equilibrium tetrahedral position. It is important to emphasize that even moderately strong CO adsorption can induce dynamic catalyst restructuring. A well-established example is the CO-driven structural evolution of Cu electrodes under CO_2RR conditions.[40] A reconstructed structure may exhibit catalytic activity that differs substantially from that of the initial geometry, and evaluating its performance would require a separate reaction-pathway calculation. In this work, we focus on the catalytic properties of the Ag_3M tetrahedral cluster in its initial configuration, and the activity of the reconstructed phase is not discussed here.

These findings show that the initial-state stability does not guarantee reaction-state stability under catalysis. The ICOHP-based cohesion mismatch parameter $|\Delta|$ serves as a bonding-imbalance indicator for the apically substituted Ag_3M@NG, capturing a cluster's resilience to adsorbate-induced perturbations. It measures the bonding disparity between the substituted Ag_b–M_a bond and the unsubstituted Ag_b–Ag_b bond; an enhanced Ag_b–M_a bond, while locally stabilizing, redistributes electron density away from the basal Ag atoms, weakening Ag_b–N anchoring and rendering the supported cluster more susceptible to adsorbate-driven structural reconstruction. Moreover, the results reveal a fundamental limitation of conventional alloying: While transition metal substitution can enhance intermediate binding and activity, it disrupts the delicate anchoring-cohesion balance underlying structural integrity. Coinage metals preserve this balance but exhibit insufficient *COOH activation (the free energy diagram of the Ag_4@NG system is shown in Fig. S5); late transition metals achieve stronger intermediate binding at the cost of reaction-state degradation. Within these apical-substitution systems, the activity-stability trade-off motivates alternative strategies to decouple these traditionally conflicting objectives.

3.4. Hydrogen-assisted electronic activation and interfacial stabilization

The findings in Subsection 3.3 reveal a dilemma: Stable coinage metal systems show insufficient *COOH activation, while reactive late-transition-metal systems suffer adsorbate-induced reconstruction. Noting that *H is ubiquitously present on electrode surfaces under cathodic potentials,[25,41] we hypothesized that a single H atom adsorbed at a well-defined hollow site on the Ag_4 cluster side face could act as an electronic promoter, simultaneously boosting both activity and stability. Figure 4(a) illustrates this Hollow-H activation model, where the H atom is positioned at a side-face hollow site of the tetrahedral cluster, coordinated by three Ag atoms (a detailed discussion of H adsorption sites on the Ag_4 cluster surface is provided in Table S3) to modulate Ag–N interfacial anchoring (via the basal Ag_3 platform) and catalytic reactivity (via the apical Ag atom). To test this, we analyzed the electronic effects of Hollow-H adsorption using PDOS and –pCOHP. The PDOS of basal Ag atoms (Fig. 4(b)) shows that H adsorption induces pronounced d-band broadening and significantly enhances states near the Fermi level (E_F). The corresponding –pCOHP analysis (Fig. 4(c)) provides quantitative evidence: The ICOHP magnitude increases from −0.35 eV (before H adsorption) to −0.56 eV (after H adsorption), an approximately 60% enhancement in Ag–N bonding strength. The enhancement stems from a substantial reduction in anti-bonding state occupation below E_F, coupled with increased anti-bonding contributions above E_F, consistent with the PDOS evidence for strengthened Ag–N hybridization.

The catalytic cycle on H-Ag_4@NG follows a distinct two-stage mechanism (Figs. 4(d) and 4(e)), differing from the conventional CO_2RR pathway on metal electrodes. Stage I (H activation): Ag_4@NG + $H^+ + e^-$ to H-Ag_4@NG, with a calculated reaction free energy of 0.80 eV. This pre-activation step, occurring prior to CO_2 admission, transforms the initially inert Ag_4@NG into the catalytically competent H-Ag_4@NG state. Stage II (CO_2RR cycle on the H-activated cluster): Starting from H-Ag_4@NG, the reaction proceeds as $^* + CO_2$ to $^*CO_2$ ($\Delta G = 0.43$ eV), $^*CO_2 + H^+ + e^-$ to *COOH ($\Delta G = -0.49$ eV), *COOH + $H^+ + e^-$ to *CO + H_2O ($\Delta G = 0.24$ eV), and *CO to CO(g) + * ($\Delta G = 0.46$ eV). The correction results of the implicit solvation model for the reaction free energy show that (Fig. S6), under both vacuum and implicit-solvent conditions the potential-determining step is H activation (stage I), not *COOH formation, making a notable departure from conventional Ag-catalyzed CO_2RR.[10,11] A direct comparison with Ag(111) is provided in Fig. S7: Hollow-H activates the Ag_4 cluster at a potential below the Ag(111) limiting potential of −0.98 V, and shifts the CO_2RR bottleneck from *COOH formation to CO desorption (0.46 eV), substantially reducing the largest free-energy uphill step within the catalytic cycle.

The Hollow-H strategy in pure Ag_4@NG is unique compared to Ag_3Cu@NG and Ag_3Au@NG (Figs. S8 and S9). While Ag_3Cu@NG has a similar H activation free-energy uphill (0.79 eV), it suffers from excessively strong intermediate binding that hinders CO desorption. Ag_3Au@NG has a lower H activation free-energy (0.37 eV) but also faces a high CO desorption energy (0.90 eV). In contrast, Ag_4@NG achieves the optimal balance with a moderate H activation energy and intermediate binding strengths (−0.49 eV to 0.46 eV for CO_2RR steps) that allow efficient CO release; a discussion of HER competition is provided in Supplementary Material Fig. S2 and Figs. S10 and S11. This aligns with design princi-

CPB Online In-Press

ples for Ag-based CO_2RR catalysts,[12] which emphasize balancing *COOH stabilization and *CO desorption. Thus, the Hollow-H acts as a dual-purpose promoter, concurrently enhancing structural stability and catalytic activity, addressing both the activity and stability issues identified in substitution engineering.

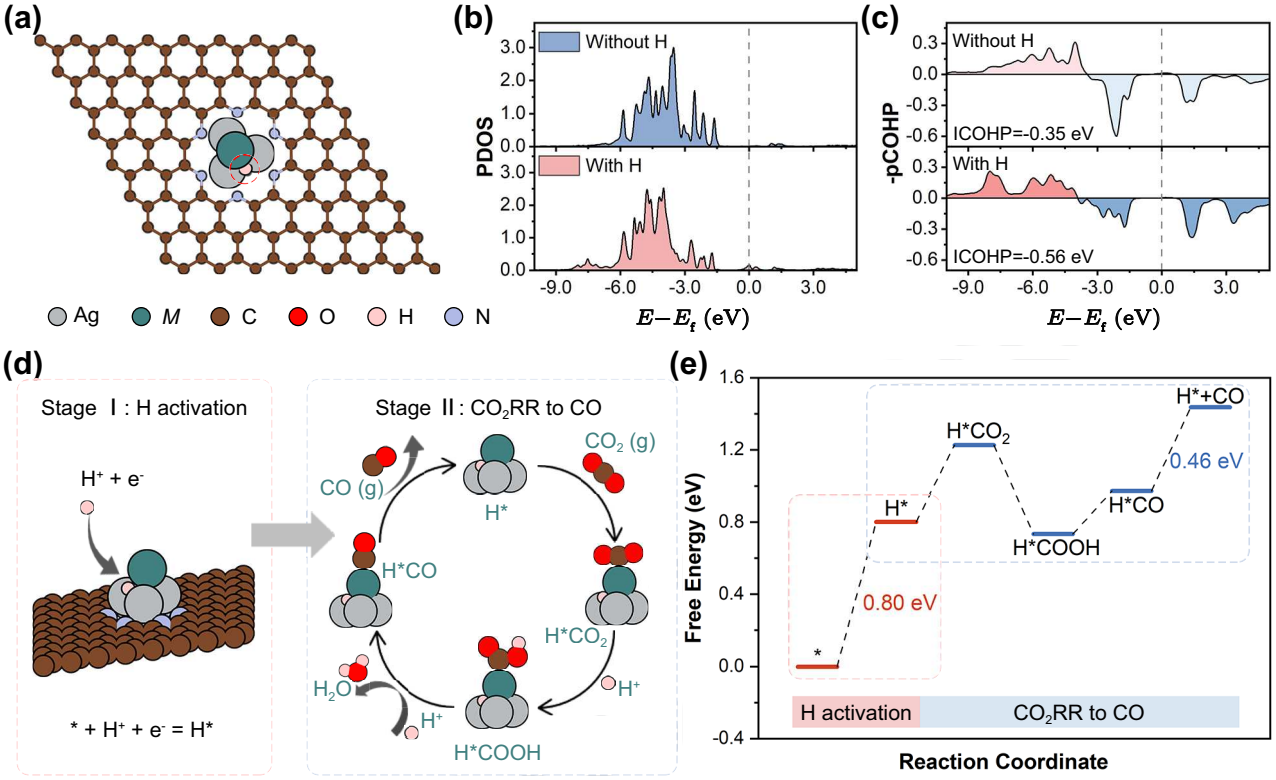


Fig. 4. Hydrogen-assisted stabilization and activation of Ag_4@NG. (a) Top-view structure of Hollow-H on Ag_4@NG, with the Hollow-H site highlighted by the red dashed circle. (b) PDOS of basal Ag atoms before (without-H) and after (with-H) Hollow-H adsorption. (c) –pCOHP of Ag–N bonds with corresponding ICOHP values. (d) Two-stage CO_2RR mechanism: H activation (Stage I, red) and CO_2RR cycle on the H-activated cluster (Stage II, blue). (e) Free energy diagram for the complete two-stage pathway of Ag_4@NG.

3.5. Hollow-H-induced dynamic charge buffer mechanism

Having established Hollow-H as a dual-purpose electronic promoter, we explore its electronic origin. Figure 5(a) presents ELF maps and CDD isosurfaces before and after H adsorption along two orthogonal cross-sections. Before adsorption, the ELF distribution is relatively isotropic in both directions. Upon Hollow-H adsorption, a pronounced anisotropy develops: Elevated ELF appears above the apical Ag atom on the side opposite to the adsorbed H (*x*-axis direction), indicating unpaired, delocalized electrons, while the *y*-axis direction remains largely unchanged. The CDD isosurfaces independently corroborate this: Before adsorption, the 3D CDD map shows net electron depletion above the apical Ag, an electronic configuration unfavorable for electrophilic CO_2RR intermediates; after adsorption, clear electron accumulation develops directly above the Ag-top, creating a polarized adsorption region primed for nucleophilic attack on incoming CO_2. Thus, Hollow-H induces directional electron polarization toward the catalytic active site. By forming a covalent bond with the side-face Ag atoms, H does not localize electron density in the Ag–H bond but triggers a global electronic polarization of the entire Ag_4 cluster, simultaneously stabilizing the side-face Ag atoms and activating the apical Ag atom for intermediate binding.

Orbital-resolved PDOS of the apical Ag (Fig. 5(b)) reveals that all five d-orbitals systematically shift toward E_F with enhanced localization. This contrasts sharply with the basal Ag atoms (Fig. 4(b)), whose d-states become more delocalized and broaden in energy. This reveals an electronic differentiation within the cluster: The basal Ag atoms, with delocalized d-orbitals, enhance hybridization with the substrate to strengthen anchoring (structural function); the apical Ag atom, with localized d-orbitals near E_F, is primed for hybridization with adsorbate orbitals (catalytic function).

The Bader charge evolution of four components along the CO_2RR pathway further illustrates this (Figs. 5(c) and 5(d)). The Ag_4 cluster continuously loses electrons, serving as the primary electron reservoir replenished by the substrate. The apical Ag atom maintains a near-constant charge, functioning as a catalytic center that facilitates directed electron flow without self-accumulation. Hollow-H continuously gains electrons, acting as a dynamic charge buffer that regulates electron release to intermediates, preventing excessive charge accumulation on the apical Ag,[26] which would weaken Ag–Ag co-

CPB Only

hesion. The reaction intermediate exhibits oscillatory charge behavior, adapting to its evolving chemical identity (* to *CO_2 to *COOH to *CO). It is this dynamic charge-buffer mechanism of Hollow-H that simultaneously activates the apical Ag site and preserves the tetrahedral structural integrity of the Ag_4 cluster throughout the CO_2RR pathway.

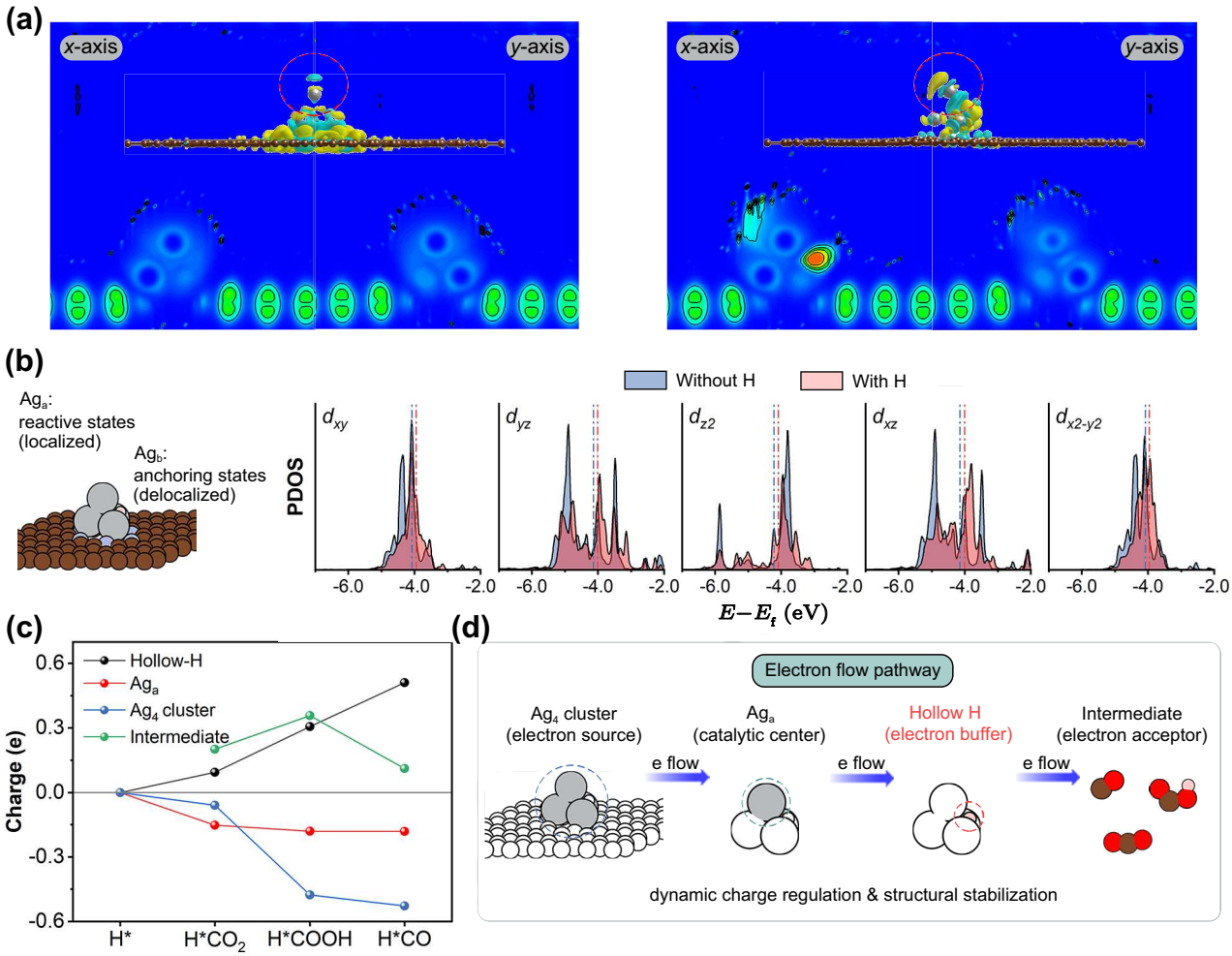


Fig. 5. Hollow-H-induced dynamic charge buffer mechanism in Ag_4@NG. (a) Left: 2D ELF maps and 3D CDD isosurfaces (isosurface = 0.0015 e/Å^3) before Hollow-H adsorption. ELF cross-sections are taken along the *x*-axis (through the Hollow-H site) and *y*-axis (perpendicular). Right: corresponding maps after Hollow-H adsorption, showing electron accumulation above the apical Ag atom along the *x*-axis direction. (b) Structure of H-Ag_4@NG and orbital-resolved PDOS of apical Ag d-orbitals, before (blue) and after (red) Hollow-H adsorption. (c) Bader charge evolution of key components along the CO_2RR pathway: Hollow-H (black), apical Ag (red), Ag_4 cluster (blue), and reaction intermediate (green). (d) Schematic of the charge buffer circuit: Ag_4 cluster to Ag_a to Hollow-H to intermediate.

4. Conclusion

We have presented a comprehensive theoretical investigation of Ag_4 clusters supported on large-pore N-doped graphene for electrochemical CO_2 reduction to CO, combining inverse-design structure search with multi-dimensional electronic structure analysis. The IM^{2}ODE algorithm identifies the regular tetrahedral Ag_4 as the most stable configuration. The stability mechanisms originate from a synergistic balance between homogeneous Ag–N interfacial anchoring (ICOHP: −0.38 eV to −0.31 eV) and uniform Ag–Ag intracluster cohesion (ICOHP: −0.29 eV to −0.23 eV). The proposed ICOHP-based cohesion mismatch parameter $|\Delta|$ serves as a bonding-imbalance indicator for structural stability under reaction. To address the activity-stability trade-off in CO_2 electroreduction, our hydrogen (Hollow-H) strategy simultaneously activates the Ag_4 cluster and reinforces interfacial Ag–N bonding through a $\sim$ 60% ICOHP enhancement. The resulting H-Ag_4@NG catalyst operates via a two-stage mechanism with H activation (0.80 eV) as the potential-determining step, a distinct departure from the *COOH-limited paradigm on conventional Ag surfaces.

Electronically, we uncover a dynamic charge buffer mechanism in which Hollow-H reorganizes the electron flow pathway as Ag_4 cluster (electron source) to apical Ag (catalytic center) to Hollow-H (dynamic buffer) to intermediate (adaptive acceptor). This strategy achieves simultaneous activity enhancement through electronic polarization of the active site and stability preservation through charge buffering that prevents accumulation-driven structural reconstruction. Whether this charge-buffer mechanism extends beyond

the present Ag_4 model to atomically precise clusters (e.g., Au_{25}, Cu_n on N-doped carbons), supports with tunable N-configurations, or reactions such as nitrate electroreduction where $^*H$ similarly governs selectivity remains an open question for experimental investigation. If confirmed, hydrogen-mediated regulation could offer a general strategy for decoupling activity and stability in supported cluster electrocatalysis.

Acknowledgments

Project supported by the National Natural Science Foundation of China (Grant Nos. 12374061 and 12404274), Zhejiang Provincial Natural Science Foundation of China (Grant No. LQN25A040020). The computations were supported by the high-performance computing center at Ningbo University.

References

[1] Seh Z W, Kibsgaard J, Dickens C F, Chorkendorff I, Nørskov J K and Jaramillo T F 2017 *Science* **355** eaad4998
[2] Nitopi S, Bertheussen E, Scott S B, Liu X, Engstfeld A K, Horch S, Seger B, Stephens I E L, Chan K, Hahn C, *et al.* 2019 *Chem. Rev.* **119** 7610
[3] Birdja Y Y, Pérez-Gallent E, Figueiredo M C, Göttle A J, Calle-Vallejo F and Koper M T M 2019 *Nat. Energy* **4** 732
[4] Ross M B, De Luna P, Li Y, Dinh C T, Kim D, Yang P and Sargent E H 2019 *Nat. Catal.* **2** 648
[5] De Luna P, Hahn C, Higgins D, Jaffer S A, Jaramillo T F and Sargent E H 2019 *Science* 364
[6] Hatsukade T, Kuhl K P, Cave E R, Abram D N and Jaramillo T F 2014 *Phys. Chem. Chem. Phys.* **16** 13814
[7] Rosen J, Hutchings G S, Lu Q, Rivera S, Zhou Y, Vlachos D G and Jiao F 2015 *ACS Catal.* **5** 4293
[8] Liu S, Tao H, Zeng L, Liu Q, Xu Z, Liu Q and Luo J L 2017 *J. Am. Chem. Soc.* **139** 2160
[9] Wang Y, Xue R, Shi C, Yan X, Shadike Z, Shen S and Zhang J 2026 *Nanoscale* **18** 10571
[10] Firet N J and Smith W A 2017 *ACS Catal.* **7** 606
[11] Vijay S, Ju W, Brückner S, Tsang S C, Strasser P and Chan K 2021 *Nat. Catal.* **4** 1024
[12] Deng X, Alfonso D, Nguyen-Phan T D and Kauffman D R 2023 *ACS Catal.* **13** 15301
[13] Qi K, Zhang Y, Li J, Charmette C, Ramonda M, Cui X, Wang Y, Zhang Y, Wu H and Wang W 2021 *ACS Nano* **15** 7682
[14] Alvarez-Gómez J M and Varela A S 2023 *Energy Fuels* **37** 15283
[15] Guo Z, Zhu H, Yang G, Wu A, Chen Q, Yan Z, Loon Fow K, Do H, Hirst J D, Wu T, *et al.* 2023 *Chem. Eng. J.* **476** 146556
[16] Zhao Z, Lin L, Ni Y, Jin L, Feng L, Wang Y, Wei Y, Zhang J and Chen J 2024 *Appl. Catal. B: Environ. Energy* **349** 123886
[17] Liu L and Corma A 2018 *Chem. Rev.* **118** 4981
[18] Yang X F, Wang A, Qiao B, Li J, Liu J and Zhang T 2013 *Acc. Chem. Res.* **46** 1740
[19] Xu Y, Zhang X, Yang C, Gong C, Qin X, Sun H, Chen H, Soldatov M A, Zheng K and Li C 2024 *Adv. Energy Mater.* 14
[20] Li M, Hu Y, Dong G, Wu T and Geng D 2023 *Small* 19
[21] Wu Z, Wang Z, She X, Shen W, Yuan J and Xu H 2024 *ChemNanoMat* 10
[22] Bai S, He Z, Zheng W, Tian Z, Jiao Z, Liu Y, Shen S and Guo L 2026 *Adv. Mater.* **38** e73318
[23] Zhang S, Liu J, Li H and Wu Y 2025 *Electrochim. Acta* **539** 147061
[24] Zhang X L, Shi Y Y, Liang X M and Li L 2025 *Mol. Catal.* **571** 114705
[25] Zhang H, Chen Y, Fang Q, Cui Y, Ren C, Li Q, Wang J and Ling C 2026 *J. Am. Chem. Soc.* **148** 20186
[26] Huang X, Wang J and Xu H 2026 *ACS Catal.* **16** 7695
[27] Zhang Y Y, Gao W, Chen S, Xiang H and Gong X G 2015 *Comput. Mater. Sci.* **98** 51
[28] Kresse G and Furthmüller J 1996 *Phys. Rev. B* **54** 11169
[29] Kresse G and Furthmüller J 1996 *Comput. Mater. Sci.* **6** 15
[30] Kresse G and Joubert D 1999 *Phys. Rev. B* **59** 1758
[31] Perdew J P, Burke K and Ernzerhof M 1996 *Phys. Rev. Lett.* **77** 3865
[32] Grimme S, Antony J, Ehrlich S and Krieg H 2010 *J. Chem. Phys.* **132** 154104
[33] Tang W, Sanville E and Henkelman G 2009 *J. Phys.: Condens. Matter* **21** 084204
[34] Deringer V L, Tchougréeff A L and Dronskowski R 2011 *J. Phys. Chem. A* **115** 5461
[35] Maintz S, Deringer V L, Tchougréeff A L and Dronskowski R 2016 *J. Comput. Chem.* **37** 1030
[36] Nørskov J K, Rossmeisl J, Logadottir A, Lindqvist L, Kitchin J R, Bligaard T and Jónsson H 2004 *J. Phys. Chem. B* **108** 17886
[37] Alonso J A 2000 *Chem. Rev.* **100** 637
[38] Chen M, Dyer J E, Li K and Dixon D A 2013 *J. Phys. Chem. A* **117** 8298
[39] Pereiro M and Baldomir D 2005 *Phys. Rev. A* **72** 045201
[40] Cheng D, Nguyen K L C, Sumaria V, Wei Z, Zhang Z, Gee W, Li Y, Morales-Guio C G, Heyde M and Roldan Cuenya B 2025 *Nat. Commun.* **16** 4064
[41] Zhang Z, Gee W, Sautet P and Alexandrova A N 2024 *J. Am. Chem. Soc.* **146** 16119

CPB Online In Press